Chemical Science

Cite this: *Chem. Sci.*, 2012, **3**, 2576

www.rsc.org/chemicalscience

EDGE ARTICLE

Experimental and quantum chemical characterization of the water oxidation cycle catalysed by $[Ru^{II}(damp)(bpy)(H_2O)]^{2+}$†

Laura Vigara,[a] Mehmed Z. Ertem,[b] Nora Planas,[b] Fernando Bozoglian,[a] Nils Leidel,[c] Holger Dau,[c] Michael Haumann,[c] Laura Gagliardi,*[b] Christopher J. Cramer*[b] and Antoni Llobet*[ade]

Received 31st March 2012, Accepted 14th May 2012
DOI: 10.1039/c2sc20399e

The water-oxidation catalytic activity of $[Ru^{II}(damp)(bpy)(H_2O)]^{2+}$ has been determined from manometric and mass spectroscopy studies. Mechanistic details of the catalytic cycle have been studied both experimentally and using DFT and CASSCF/CASPT2 calculations. Characterisation of this Ru(II) complex and more highly oxidized catalytic intermediates has been accomplished through UV-vis and XAS spectroscopy, as well as through electrochemical techniques. Comparison of XAS spectra with CASSCF/CASPT2 calculations provides insight into the electronic structures of the more highly oxidized species, especially the degree to which oxidation occurs over both atoms of the Ru–O fragment. ^{18}O-labelling experiments indicate that the O–O bond formation step proceeds *via* a water nucleophilic attack mechanism, and a detailed DFT analysis of the catalytic cycle predicts that step to be rate-determining and to take place for a formal Ru(V)=O species. A number of alternative higher energy pathways have also been characterised in order to provide a more complete vision of the whole system.

Introduction

Hydrogen is a clean fuel that is attracting substantial attention from heavily consuming energy related industrial sectors such as auto manufacturers. The H_2-based technology is already highly developed and can be used to provide electricity to a house or car and also produce hot water or run domestic central heating. Particularly interesting is the Personal Power Plant (P3) concept that was put forward in 1994 by Honda[1] and more recently by Audi.[2] However, while significant progress in the storage and use of hydrogen has already been achieved,[3] the question of how to obtain a sustainable hydrogen source still remains to be answered.[4] One attractive solution consists of achieving water splitting by sunlight. An advantage of solar-derived H_2 relative to direct solar electricity generation is that stored H_2 fuel can be used independently of the planet's rotational position. In order efficiently to transform solar photons into chemical energy, robust and fast water oxidation catalysts are needed. Many transition metal complexes have been reported that can oxidize water to dioxygen,[5] and a few detailed mechanistic studies have been performed.[6] Of those studies, the majority have focused upon Ru complexes. Understanding potential reaction pathways, as well as deactivation pathways, is a crucial first step in the design of next-generation catalysts that can be used practically in a commercial water-splitting cell.

We report here the characterization of a mononuclear Ru complex $[Ru^{II}(damp)(bpy)(H_2O)]^{2+}$, (damp is 2,6-bis((dimethylamino)methyl)pyridine and bpy is 2,2′-bipyridine; see Chart 1 for a drawing of the ligands), hereafter known as $[Ru^{II}–OH_2]^{2+}$ or $\mathbf{1}^{2+}$, a compound that has previously been reported but not with respect to its higher oxidation states and activity as a water oxidation catalyst. With an ^{18}O labelling study we unambiguously show that water nucleophilic attack (WNA) is the mechanism employed by the catalyst for O–O bond formation. In addition, a stepwise microscopic mechanistic pathway is proposed on the basis of density functional theory (DFT) calculations, with all intermediate and transition-state structure energetics determined to be consistent with experimental

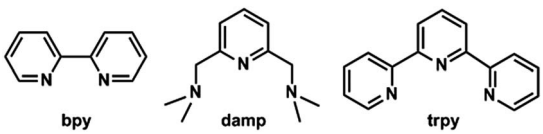

Chart 1 The ligands.

[a]*Institute of Chemical Research of Catalonia (ICIQ), Av. Països Catalans 16, E-43007 Tarragona, Spain. E-mail: allobet@iciq.es*
[b]*Department of Chemistry and Supercomputing Institute, University of Minnesota, 207 Pleasant St. SE, Minneapolis, MN 55455-0431, USA. E-mail: gagliard@umn.edu; cramer@umn.edu*
[c]*Institut für Experimentalphysik, Freie Universität Berlin, Arnimallee 14, D-14195 Berlin, Germany. E-mail: haumann@zedat.fu-berlin.de*
[d]*Departament de Química, Universitat Autònoma de Barcelona, Cerdanyola del Vallès, E-08193 Barcelona, Spain*
[e]*Department of Bioinspired Science, Ewha Womens University, 120-750 Seoul, Korea*
† Electronic supplementary information (ESI) available: Additional computational details. See DOI: 10.1039/c2sc20399e

observations. Finally, multireference calculations followed by second order perturbation theory (CASPT2) on compound $\mathbf{1}^{2+}$ and its more highly oxidized analogues are analysed to describe the character of the Ru–O moiety in the different oxidation states.

Experimental and computational methods

Materials

Trifluoromethanesulfonic acid (99+%) was purchased from STREM/CYMIT. All other chemicals used in the present work were supplied by Aldrich Chemical Co. in the highest purity commercially available and were used without further purification. Reagent grade organic solvents were obtained from SDS. High purity de-ionized water was obtained by passing distilled water through a nano-pure Milli-Q water purification system. The complex $[Ru^{II}(damp)(bpy)(H_2O)]^{2+}$, $[Ru^{II}–OH_2]^{2+}$ or $\mathbf{1}^{2+}$, was prepared following literature procedures.[27]

Manometric measurements

On-line manometric measurements were carried out on a Testo 521 differential pressure manometer with an operating range of 1–100 hPa and accuracy within 0.5% of the measurement. The manometer was coupled to a thermostated reaction vessel for dynamic monitoring of the headspace pressure above each reaction. The manometer's secondary ports were connected to a thermostated reaction vessel containing the same solvent and headspace volumes as the sample vials.

Spectrophotometric titrations

UV-vis spectroscopy was performed on a Cary 50 (Varian) UV-vis spectrophotometer in Standard 1 cm Quartz cuvettes. Redox spectrophotometric titrations were performed by sequential addition of a small volume of a freshly prepared aqueous 5 mM solution of $(NH_4)_2[Ce(NO_3)_5]$ (Ce(IV)) in an aqueous 0.1 M CF_3SO_3H to a $[Ru^{II}–OH_2]^{2+}$ complex solution (0.1 mM) also in 0.1 M CF_3SO_3H.

Kinetics

Experiments were performed on a Cary 50 spectrophotometer from Varian equipped with a temperature-controlled cell holder. In a typical experiment, to a 3 mL solution of 4 mM Ru(II) complex in 0.1 M CF_3SO_3H were added 25 μL of 0.1 M triflic acid solution containing 3 equivalents of Ce(IV). The temperature of the system was maintained at 25.0 ± 0.1 °C. The reaction was monitored by recording spectra in the 350–600 nm range every 30 s for 120 min.

Experimental data was fitted to two consecutive second and first order reaction models (A + B → C → D) by a global fitting method using Specfit.[33] Errors shown correspond to one σ of the fitting with respect to experimental points.

Electrochemistry

Cyclic voltammetry (CV) and square wave voltammetry (SQWV) experiments were performed in an IJ-Cambria CHI-660 potentiostat using a three electrode cell. A glassy carbon disk electrode (2 mm diameter) was used as working electrode, platinum wire as auxiliary and SSCE as the reference electrode. Typical CV experiments were carried out at a scan rate of 100 mV s^{-1}. SQWV experiments were performed with the following parameters: Scan rate = 100 mV s^{-1}, SW amplitude = 50 mV and SW frequency = 2 Hz. $[Ru^{II}–OH_2]^{2+}$ complex (0.20 mM) was dissolved in 0.1 M CF_3SO_3H solution (pH 1.0). $E_{1/2}$ values reported in this work were estimated from CV as the average of the oxidative and reductive peak potentials $(E_{p,a} + E_{p,c})/2$ or taken as $E(I_{max})$ from SQWV measurements.

^{18}O labelling

In a typical experiment, 0.75 mL of a 0.010 M solution of $[Ru^{II}–OH_2]^{2+}$ in $H_2{}^{16}O$ (7.5 μmol) were introduced into a flask followed by the addition of 0.25 mL of a 0.06 M $(NH_4)_2Ce(NO_3)_6$ (15 μmol) solution in $H_2{}^{16}O$. The solution is stirred for a few seconds and a further addition of 0.25 mL of a 0.06 M Ce(IV) (15 μmol) solution in $H_2{}^{18}O$ (water ^{18}O, 97%, Cambridge Isotope Laboratories, Inc.) were added. This produces a final concentration of catalyst of 6.0 mM and a final $H_2{}^{18}O$ content of 19.40%. The composition of the gas phase ($^{16}O_2$, m/z = 32; $^{16}O^{18}O$, m/z = 34 and $^{18}O_2$, m/z = 36) was monitored on-line by an Omnistar™ GSD 301 C (Pfeiffer) quadrupole mass spectrometer apparatus.

X-ray absorption spectroscopy (XAS)

XAS at the ruthenium K-edge was performed at the Super XAS beam line at Swiss Light Source (SLS at Paul Scherrer Institut, Villigen, Switzerland) as previously described.[7] K_α-fluorescence-detected XAS spectra were measured with an energy-resolving 13-element Ge-detector (Canberra) on samples held in a liquid-helium cryostat (Oxford) at 20 K, using excitation by X-rays from a double-crystal Si[311] monochromator. Energy calibration of each scan was done using the first inflection point at 22117 eV in the absorption spectrum of a Ru–metal powder sample as a standard. 5–7 scans were averaged, normalized, and Extended X-ray Absorption Fine Structure (EXAFS) spectra were derived as described previously.[8] EXAFS simulations were carried out using the software SimX and phase functions calculated with FEFF8.[9]

Density functional theory

All geometries were fully optimized at the M06-L level[10] of density functional theory using the Stuttgart [8s7p6d2f|6s5p3d2f] ECP28MWB contracted pseudopotential basis set[11] on Ru and the 6-31G(d) basis set[12] on all other atoms. Non-analytical integral evaluations made use of a pruned grid having 99 radial shells and 590 angular points per shell and an automatically generated density-fitting basis set was used within the resolution-of-the-identity approximation to speed the evaluation of the Coulomb integrals. The nature of all stationary points was verified by analytical computation of vibrational frequencies, which were also used for the computation of zero-point vibrational energies, molecular partition functions (with all frequencies below 50 cm^{-1} replaced by 50 cm^{-1} when computing free energies), and for determining the reactants and products associated with each transition-state structure (by following the

normal modes associated with imaginary frequencies). Partition functions were used in the computation of 298 K thermal contributions to free energy employing the usual ideal-gas, rigid-rotator, harmonic oscillator approximation.[13] Free energy contributions were added to single-point M06-L electronic energies computed with the SDD basis set on ruthenium and the 6-311+G(2df,p) basis set on all other atoms to arrive at the final, composite, gas-phase free energies.

Solvation and standard reduction potentials

Solvation effects associated with water as solvent were accounted for using the SMD continuum solvation model.[14] A 1 M standard state was used for all species in aqueous solution except for water itself, for which a 55.6 M standard state was employed. Thus, for all molecules but water, the free energy in aqueous solution is computed as the 1 atm gas-phase free energy, plus an adjustment for the 1 atm to 1 M standard-state concentration change of $RT\ln(24.5)$, or 1.9 kcal mol^{-1}, plus the 1 M to 1 M transfer (solvation) free energy computed from the SMD model. In the case of water, the 1 atm gas-phase free energy is adjusted by the sum of a 1 atm to 55.6 M standard-state concentration change, or 4.3 kcal mol^{-1}, and the experimental 1 M to 1 M solvation free energy, −6.3 kcal mol^{-1}. The 1 M to 1 M solvation free energy of the proton was taken from experiment as −265.9 kcal mol^{-1}.[15]

Standard reduction potentials were calculated for various possible redox couples to assess the energetic accessibility of different intermediates at various oxidation states. For a redox reaction of the form

$$O_{(aq)} + ne^-_{(g)} \rightarrow R_{(aq)} \quad (1)$$

where O and R denote the oxidized and reduced states of the redox couple, respectively, and n is the number of electrons involved in redox reaction. The reduction potential $E^{o}_{O|R}$ relative to the standard hydrogen electrode (SHE) was computed as

$$E^{o}_{O|R} = -\frac{\Delta G^{o}_{O|R} - \Delta E^{o}_{SHE}}{nF} \quad (2)$$

where $\Delta G^{o}_{O|R}$ is the free energy change associated with eqn (1) (using Boltzmann statistics for the electron), and $\Delta G^{o}_{SHE}$is the free energy change associated with

$$H^+_{(aq)} + e^-_{(g)} \rightarrow \frac{1}{2}H_{2(g)} \quad (3)$$

which is −4.28 eV with Boltzmann statistics for the electron,[15c,16] and F is the Faraday constant.

Non-single-determinantal state energies

Several possible intermediates in the water oxidation mechanism have electronic structures that are not well described by a single determinant. In such instances, standard Kohn–Sham DFT is not directly applicable,[13,17] and we adopt the Yamaguchi broken-spin-symmetry (BS) procedure[18] to compute the energy of the spin-purified low-spin (LS) state as

$$^{LS}E = \frac{^{BS}E(^{HS}\langle S^2\rangle - ^{LS}\langle S^2\rangle) - ^{HS}E(^{BS}\langle S^2\rangle - ^{LS}\langle S^2\rangle)}{^{HS}\langle S^2\rangle - ^{BS}\langle S^2\rangle} \quad (4)$$

where HS refers to the single-determinantal high-spin coupled state that is related to the low-spin state by spin flip(s) and $\langle S^2\rangle$ is the expectation value of the total spin operator applied to the appropriate determinant. This broken-symmetry DFT approach has routinely proven effective for the prediction of state-energy splittings in metal coordination compounds.[17b,20]

Multiconfigurational calculations

Multireference calculations based on the CASSCF and CASPT2[21] methods, were performed for system **1** in oxidation states ranging from II to VI. The calculations were performed at the DFT ground state optimized geometries. All CASSCF/CASPT2 calculations made use of the MOLCAS version 7 program suite.[22] Scalar relativistic effects were included by use of the Douglas–Kroll–Hess Hamiltonian to second order[23] and the relativistic all-electron ANO-RCC[24] basis sets using a triple-ζ quality (ANO-RCC-VTZP) [7s6p4d2f1g] contraction for Ru, a double-ζ quality (ANO-RCC-VDZP) [3s2p1d] contraction for O and N, and the minimal [1s] and [2s2p] ANO-RCC-MB basis set for H and C. Several CASSCF active spaces were tested. Ultimately, for the deprotonated higher oxidation states IV, V and VI, we choose an active space containing ten, nine and eight electrons, respectively, in eight orbitals, corresponding to linear combinations of four of the 4d orbitals of Ru (containing 0, 1 and 2 electrons going from oxidation state VI to IV), the valence orbitals of the O atom (6 electrons) and one 2p orbital of one of the N atoms on the damp ligand (2 electrons). The remaining 4d doubly occupied orbitals are significantly lower in energy, and we thus did not include them in the active space.

In the lower spin species containing "aqua" ligands there is no Ru=O π bond and thus the most reasonable active space includes 5/6 electrons (for oxidation states III and II) in 5 orbitals, corresponding to the linear combination of three Ru 4d orbitals (containing 1 and 2 electrons, respectively, for oxidation states II and III), one doubly occupied sp^2 orbital of the O atom (2 electrons) and one 2p orbital of one of the N atoms on the DAMP ligand (2 electrons). All systems were found to be essentially single-configurational. As part of that analysis, Loprop[25] population analyses were performed using the CASSCF density for the different oxidation states. The natural orbital occupation numbers were used for the evaluation of the effective bond order (EBO),[26] between Ru and O in the different oxidation states of system **1** which is calculated as one half the difference between the total occupancies of the bonding and antibonding molecular orbitals of the Ru–O bond.

Results and discussion

The complex $[Ru^{II}(damp)(bpy)(OH_2)]^{2+}$, $[Ru^{II}–OH_2]^{2+}$ or $\mathbf{1}^{2+}$, was prepared and partly characterized by the Thorp group[27] in 1997.

The damp ligand, containing two strongly σ-donating tertiary amine coordinating groups, provides the right electronic environment to stabilize higher oxidation states. As a consequence, diffraction quality monocrystals of the $[Ru^{IV}=O]^{2+}$ complex can be obtained at 4 °C. A computed structure for the $[Ru^{IV}=O]^{2+}$ complex is represented in Fig. 1 that has very similar bond distances and angles, to that of the X-ray structure as will be

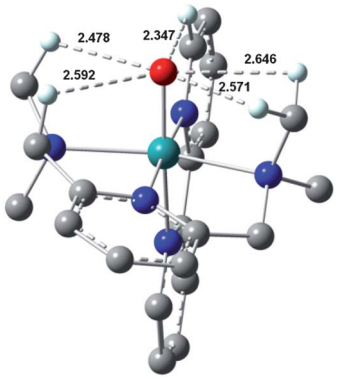

Fig. 1 DFT optimized structure for $[Ru^{IV}{=}O]^{2+}$ showing the H-bonding network for the O-atom of the Ru–O group.[19]

discussed below. Stabilization of the higher oxidation states was also corroborated by cyclic voltammetry (CV) where roughly a 200 mV cathodic shift is observed for both couples, the IV/III and the III/II, compared to the analogous benchmark Ru-aqua complex $[Ru^{II}(trpy)(bpy)(OH_2)]^{2+}$, (trpy is 2,2':6',2"-terpyridine), $\mathbf{2}^{2+}$ (see Table 1). Further, the crystal structure of the $[Ru^{IV}{=}O]^{2+}$ complex shows extensive C–H···O hydrogen bonding between the oxo group and the H atoms of the methyl and methylene groups of damp as well as one C–H pyridyl, as can be observed in the computed structure (Fig. 1). This H-bonding phenomenon can influence the reactivity of $\mathbf{1}^{2+}$, especially with regard to its ability to catalytically oxidize water to molecular oxygen, since the Ru–O is the site of the molecule where the critical chemistry occurs.

UV-vis spectroscopy and kinetics

The UV-vis spectra of complex $[Ru^{II}–OH_2]^{2+}$ and its higher oxidation states, generated by sequential addition of the corresponding equivalents of Ce(IV) at pH = 1.0 are presented in Fig. 2. The spectra for Ru(II), Ru(III) and Ru(IV) have been previously reported and will not be further discussed here. One

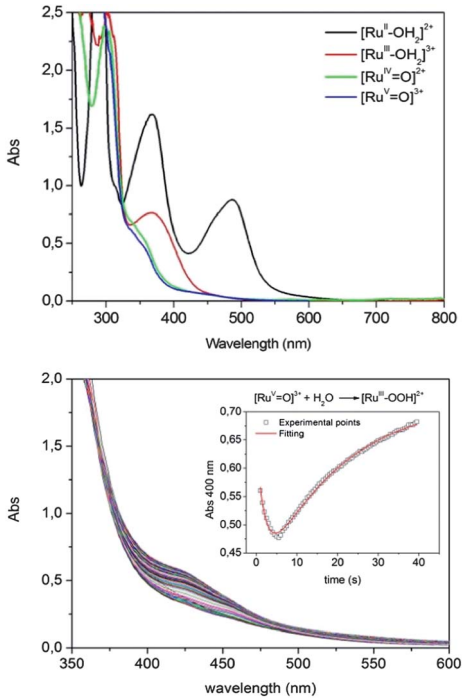

Fig. 2 Top, UV-vis spectra for 0.1 mM $[Ru^{II}–OH_2]^{2+}$, and their higher oxidation state species obtained by the addition of the corresponding equivalents of Ce(IV), $[Ru^{III}–OH_2]^{3+}$, $[Ru^{IV}{=}O]^{2+}$ and $[Ru^{V}{=}O]^{3+}$ registered at pH = 1.0 in a 0.1 M triflic acid solution. Bottom, generation of $[Ru^{V}{=}O]^{3+}$ by adding 3 equivalent of Ce(IV) to a 4.0 mM of $[Ru^{II}–OH_2]^{2+}$ and its evolution over time to $[Ru^{III}–OOH]^{2+}$. The inset shows the absorption evolution of $\lambda_{400\ nm}$ over time (empty black squares) and its mathematical fit (solid red line).

Table 1 Redox potentials *vs.* NHE and kinetic data for $\mathbf{1}^{2+}$ and selected $Ru–OH_2$ complexes at pH = 1.0

Complex[a]	$E_{1/2}$ *vs.* NHE			Rate constants			
	III/II	IV/III	V/III	$k_{IV–V}$ ($M^{-1}\ s^{-1}$)[f]	$k_{O–O}$ (s^{-1})[g]	rds-reaction[e] (rate constant)	ref
$[Ru(damp)(bpy)(H_2O)]^{2+}$, $\mathbf{1}^{2+}$	0.83	>0.97[b]	1.79	1.38	2.0×10^{-3}	$[Ru^{V}{=}O]^{2+} + H_2O \rightarrow [Ru^{III}–OOH]^{2+}$	this work
$[Ru(trpy)(bpy)(H_2O)]^{2+}$, $\mathbf{2}^{2+}$	1.04 (1.01)[c]	1.23 (1.19)[c]	1.80 (1.60)[c]	—	—	$[Ru^{IV}–OO]^{2+} + H_2O \rightarrow [Ru^{II}–OH_2]^{2+} + O_2$ [h] ($1.9 \times 10^{-4}\ s^{-1}$)	6b(30)
$[Ru(trpy)(bpm)(H_2O)]^{2+}$, $\mathbf{3}^{2+}$	1.12[d]		1.65	5.0	9.6×10^{-3}	$[Ru^{IV}–OO]^{2+} + H_2O \rightarrow [Ru^{II}–OH_2]^{2+} + O_2$ ($5.7 \times 10^{-4}\ s^{-1}$)	6a
$[Ru(trpy)(bpz)(H_2O)]^{2+}$, $\mathbf{4}^{2+}$	1.22[d]		1.69	—	1.4×10^{-3}	$[Ru^{IV}–OO]^{2+} + H_2O \rightarrow [Ru^{II}–OH_2]^{2+} + O_2$	30
$[Ru(trpy)(MeO\text{-}bpy)(H_2O)]^{2+}$, $\mathbf{5}^{2+}$	0.91	1.24	1.77	3.7	3×10^{-5}	$[Ru^{IV}–OO]^{2+} + Ce^{IV} \rightarrow [Ru^{V}–OO]^{3+} + Ce^{III}$ ($1.0\ M^{-1}\ s^{-1}$)	6b
$[Ru(trpy)(Hbpp)(H_2O)]^{2+}$, $\mathbf{6}^{2+}$	0.91	1.24	1.70	disprop[i]	1.8×10^{-3}	$[Ru^{V}{=}O]^{2+} + H_2O \rightarrow [Ru^{III}–OOH]^{2+}$ and $[Ru^{IV}–OO]^{2+} + H_2O \rightarrow [Ru^{II}–OH_2]^{2+} + O_2$ ($2.7 \times 10^{-3}\ s^{-1}$)	5b
$[Ru(trpy)(acac)(H_2O)]^{+}$, $\mathbf{7}^{+}$	0.51	1.14	1.58	515	5.0×10^{-4}	—	30

[a] Ligand abbreviations: bpm, 2,2′-bipyrimidine; bpz, 2,2′-bipyrazine; MeO-bpy, 4,4′-dimethoxy-2,2′-bipyridine; Hbpp, 3,5-bis(2-pyridyl)pyrazole. [b] Assuming a $pK_{a,III} > 1.8$ and taking into consideration that the $\Delta E_{(IV,III–III,II)}$ is 140 mV at pH = 7.0. [c] In parenthesis are the values reported in ref. 23. [d] This value corresponds to a two electron wave for the couple Ru(IV)/Ru(II). [e] rds stands for rate determining step. [f] $k_{IV–V}$ ($M^{-1}\ s^{-1}$) is the rate constant for the reaction $Ru^{IV}{=}O + Ce^{IV} \rightarrow Ru^{V}{=}O + Ce^{III}$. [g] $k_{O–O}$ (s^{-1}) is the rate constant for the reaction $[Ru^{V}{=}O]^{2+} + H_2O \rightarrow [Ru^{III}–OOH]^{2+}$. [h] For this complex the rds switches to $[Ru^{IV}–OO]^{2+} + Ce^{IV} \rightarrow [Ru^{V}–OO]^{3+} + Ce^{III}$ when the pH is changed to 0.0. [i] Ru(V) is proposed to be generated by the disproportion of Ru(IV).

interesting feature of this complex is its capacity to achieve oxidation state v, as has been observed for related complexes.[28,29,30,31] A feature that significantly differentiates these higher oxidation states is their relative stability. As already mentioned above, complex $\mathbf{1}^{2+}$ at oxidation state IV, $[Ru^{IV}{=}O]^{2+}$, is stable at 4 °C, although it slowly deactivates at room temperature. In sharp contrast, at oxidation state v, $[Ru^{V}{=}O]^{3+}$, the complex reacts quickly with water to generate the corresponding hydroperoxide species, $[Ru^{III}{-}OOH]^{2+}$, according to the following equations,

$$[Ru^{IV}{=}O]^{2+} + Ce(IV) \rightarrow [Ru^{V}{=}O]^{3+} + Ce(III) \quad (5)$$

$$[Ru^{V}{=}O]^{3+} + H_2O \rightarrow [Ru^{III}{-}OOH]^{2+} + H^+ \quad (6)$$

The formation of the O–O bond according to eqn (6) is known as the water nucleophilic attack mechanism (WNA) that will be discussed in further sections.[32]

Kinetic analyses for these reactions were carried out, monitored by UV-vis spectroscopy and are shown in Fig. 2. Mathematical treatment with Specfit[33] of the spectroscopic traces assuming a second order rate constant for k_{IV-V} (1.38 $M^{-1}s^{-1}$; eqn (5)) and pseudo first order for k_{O-O} (2.0×10^{-3} s^{-1}; eqn (6)), gives a very nice fit as can be observed in the inset of Fig. 2. Similar processes for related mononuclear Ru complexes have been reported in the literature and are presented in Table 1. For both complexes $\mathbf{3}^{2+}$ and $\mathbf{5}^{2+}$ containing the bpm (bpm is 2,2′-bipyrimidine) and the MeO-bpy (4,4′-dimethoxy-2,2′-bipyridine) ligands, respectively, their k_{IV-V} rate constants are within the same order of magnitude as for $\mathbf{1}^{2+}$. However for $\mathbf{7}^{+}$, that contains the anionic and strongly σ-donating ligand acac (acac is acetylacetonato) this rate constant increases by more than two orders of magnitude.

With regard to the k_{O-O}, it is interesting to observe that complex $\mathbf{4}^{2+}$, containing the electron withdrawing 2,2′-bipyridazine ligand (bpz), has a rate constant that is very similar to that of $\mathbf{1}^{2+}$. In sharp contrast, the same constant displays a high sensitivity to electronic effects for complexes $\mathbf{3}^{2+}$ and $\mathbf{5}^{2+}$ differing by more than two orders of magnitude. In $\mathbf{3}^{2+}$, containing the electron withdrawing bpm ligand, the rate increases up to 9.6×10^{-3} s^{-1}, whereas in $\mathbf{5}^{2+}$, containing the electron donating MeO-bpy ligand, it decreases to 3×10^{-5} s^{-1}.

X-ray absorption spectroscopy

XAS measurements were carried out to derive structural and electronic information related to Ru–O type of complexes. For this purpose, the damp complex $[Ru^{II}{-}OH_2]^{2+}$, $\mathbf{1}^{2+}$, and its higher oxidation state species, $[Ru^{III}{-}OH_2]^{3+}$ and $[Ru^{IV}{=}O]^{2+}$ were prepared in aqueous solution in 0.1 M triflic acid, by the addition of the corresponding equivalents of Ce(IV). Their XAS spectra are shown in Fig. 3. The X-ray Absorption Near Edge Structure (XANES) spectra reveal an up-shift of the Ru K-edge energy of ~0.9 eV associated with the Ru(II) → Ru(III) transition and a ~0.6 eV edge shift for the Ru(III) → Ru(IV) transition (Fig. 3A). This lower edge shift value for the latter case indicates that the oxidation is taking place both at the metal center and the oxygen atom of the Ru–O group. An unweighted valence bond

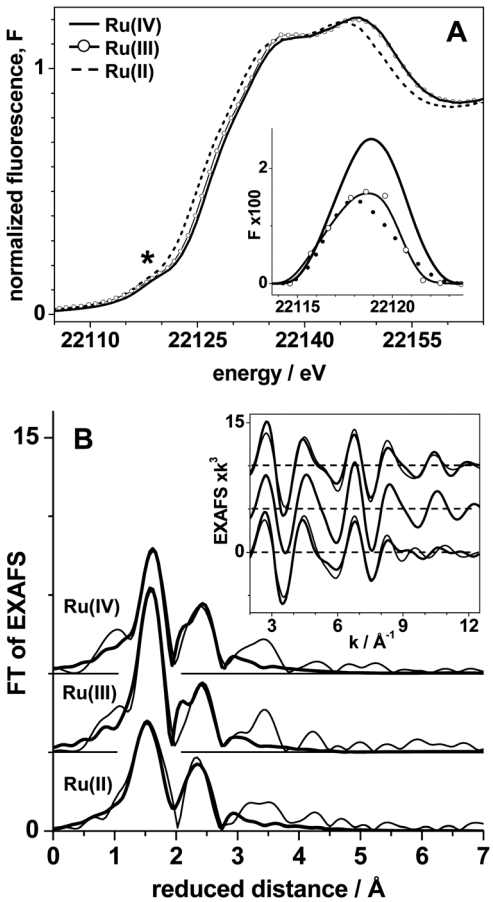

Fig. 3 XAS spectra for $\mathbf{1}^{2+}$ and its higher oxidation states III and IV. (A) Ru XANES spectra and K-edge energies and isolated pre-edge features (asterisk) in the inset (Table 2). (B) Fourier-transforms (FTs) of EXAFS spectra. FTs were calculated for *k*-values of 2–12.5 $Å^{-1}$ and using $\cos^2$ windows over 10% of both *k*-range ends. The inset contains Fourier-filtered *k*-space data corresponding to back transforms of FTs over 1–3 Å of reduced distance. Thick lines: simulations with parameters that are presented in Table 2. Thin lines: experimental data. FT and *k*-space spectra were vertically displaced for comparison.

formulation for this species can be represented as $[Ru^{IV}{=}O \leftrightarrow Ru^{III}{-}O^{\cdot}]$, as we have been previously proposed for the higher oxidation states of the *cis*-$[Ru^{II}(bpy)_2((H_2O)_2]^{2+}$ complex.[34c] This description can also be applied to other Ru–OH_2 type of complexes in oxidation states higher than III.[34] The EXAFS results further support this description since the pre-edge peak area (inset Fig. 3A) for $[Ru^{IV}{=}O]^{2+}$ is almost doubled compared to the one for $[Ru^{III}{-}OH_2]^{3+}$. This increase in pre-edge peak area is a clear indication of a significantly higher double bond character. EXAFS spectra (inset Fig. 3B) were well simulated by the inclusion of first sphere Ru–O and Ru–N and second sphere Ru···C distances. The determined bond lengths are summarized in Table 2. As can be seen in the Table the increase in oxidation state produces a decrease of the Ru–O bond length, especially for $[Ru^{IV}{=}O]^{2+}$, and a slight decrease of the Ru–N bond length. For the Ru(IV) sample a satisfactory fit required the inclusion of two Ru–N distances differing by ~0.14 Å. The predominance of Ru(IV)=O in the sample is in agreement with the considerable K-edge shift.

Table 2 Ruthenium-ligand distances for $\mathbf{1}^{2+}$ and its higher oxidation states from EXAFS analysis and their edge energies and pre-edge areas from XANES spectra

	EXAFS					XANES	
Oxidation state	Ru=O *n* [per Ru]/*R* [Å]/$2\sigma^2 \times 10^3$ [Å^2][a]	Ru–O/N	Ru–N	Ru–C	R_F [%][b]	E_{edge} [eV]	$A_{pre\text{-}edge}$ [r.u.][d]
Ru(II)	—	1/2.18/2	5/2.04/13	12/2.95/20	26.4	22124.9	0.55
Ru(III)	—	1/2.13/2	5/2.04/8	12/2.98/20	23.0	22125.8	0.63
Ru(IV)	1/1.77/2	—	5/2.06/16	12/2.96/22	45.0	22126.4	1.00
	1/1.78/2	2.60[c]/1.99/2	2.40[c]/2.14/2	12/2.96/22	27.8		

[a] *n*, number of atoms surrounding the metal center (coordination number). *R*, is the distance between Ru and the atoms situated at its first and second coordination sphere. $2\sigma^2$, is the Debye–Waller parameter. All coordination numbers (*n*) were fixed at their chemical values in the simulations except in the case indicated in c. [b] R_F, error sum[8] calculated over reduced distances of Fourier-transforms of 1–3 Å. [c] Values coupled to yield a sum of 5; $2\sigma^2$ of the Ru=O bond was fixed to 0.002 Å^2 in the simulations.

Electrochemical characterization

Electrochemical experiments were carried out by means of Cyclic Voltammetry (CV) and Square Wave Voltammetry (SQWV) and the voltammograms are shown in Fig. 4. Previous electrochemical work[27] for complex $\mathbf{1}^{2+}$ showed the presence of two PCET waves at pH = 7.0 associated with,

$$[Ru^{III}\text{–}OH]^{2+} + 1H^+ + 1e^- \rightarrow [Ru^{II}\text{–}OH_2]^{2+}\ E^{o}_{III/II}\ (pH, 7) = 0.30\ vs.\ SSCE\ (0.536\ vs.\ NHE) \quad (7)$$

$$[Ru^{IV}{=}O]^{2+} + 1H^+ + 1e^- \rightarrow [Ru^{III}\text{–}OH]^{2+}\ E^{o}_{III/II}\ (pH, 7) = 0.44\ vs.\ SSCE\ (0.676\ vs.\ NHE) \quad (8)$$

These redox couples are 160 and 140 mV lower than the same processes for $\mathbf{2}^{2+}$ respectively, as a consequence of replacing the π-acceptor trpy ligand by the weaker π-acceptor and stronger σ-donating damp ligand. Furthermore, this effect also impacts their acidity that is manifested in an increase of nearly two orders of magnitude of the $pK_{a,II}$ values (11.5 for $\mathbf{1}^{2+}$; 9.7 for $\mathbf{2}^{2+}$). At low pH, only the III/II wave is observed and the $pK_{a,III}$ has not been calculated. However the latter is also expected to suffer a significant increase with regard to $\mathbf{2}^{2+}$, which has a pK_a of 1.7.[35] The CV and SQWV at pH = 1.0 are shown in Fig. 4 where the III/II couple appears at 0.60 V *vs.* SSCE (0.836 *vs.* NHE). The IV/III is not observed and finally a new redox process with a large electrocatalytic current is observed that is associated with the generation of Ru(V) (eqn (5)). The reaction of Ru(V) with H_2O to produce the Ru(III)–OOH (eqn (6)) and the combination of reactions that lead to the formation of dioxygen (eqns (9), (10)).

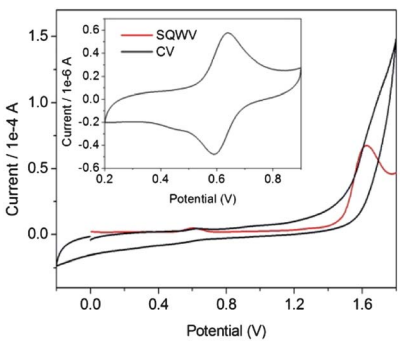

Fig. 4 Black line, CV of $\mathbf{1}^{2+}$ at pH = 1.0 in a 0.1 M triflic acid solution at 100 mV s^{-1} scan rate using Pt wire as auxiliary electrode and SSCE as reference electrode. Red line, SQWV of $\mathbf{1}^{2+}$. The inset shows the CV of $\mathbf{1}^{2+}$ within the 0.2–0.9 V potential window.

$$[Ru^{III}\text{–}OOH]^{2+} - 1e^- - 1H^+ \rightarrow [Ru^{IV}\text{–}OO]^{2+} \quad (9)$$

$$[Ru^{IV}\text{–}OO]^{2+} + H_2O \rightarrow [Ru^{II}\text{–}OH_2]^{2+} + O_2 \quad (10)$$

This establishes the electrocatalytic cycle, as proposed by DFT analysis that is described in the following section.

O_2 evolution and labelling

Addition of an excess of a strong oxidant such as Ce(IV) at pH = 1.0 to a dilute solution of $\mathbf{1}^{2+}$ produces molecular oxygen, that was monitored by manometry and on-line MS. The system of $\mathbf{1}^{2+}$ 1.0 mM/Ce(IV) 100 mM in 2.0 mL of 0.1 M triflic acid solution at 298 K gave 9.4 μmols of O_2 that represents a Turnover Number (TON) of 4.6 with a Turnover Frequency (TOF) of 3.7 h^{-1}, as shown in Fig. 5. The efficiency with regard to the Ce(IV) oxidant is only 18.8% indicating that probably other oxidative process besides water oxidation are also occurring with deactivation of the water oxidation capacity of the catalyst. On line MS showed only trace amounts of CO_2. The inset of Fig. 5 shows the manometric response when the ratio of Ce(IV)/$\mathbf{1}^{2+}$ is set at 4.1. In this case 0.22 TONs were achieved that represents a slight increase of oxidative efficiency with regard to the previous case.

These experiments together with the stability of the $[Ru^{IV}{=}O]^{2+}$ high oxidation state and the reactivity of $[Ru^{V}{=}O]^{3+}$ indicate that this is an excellent system to study mechanistically. Indeed labelling experiments were carried out using 6.0 mM $\mathbf{1}^{2+}$ in H_2O^{16} and adding 2 equivalents of Ce(IV) to generate $[Ru^{IV}{=}O]^{2+}$, then two more equivalents of Ce(IV) dissolved in H_2O^{18} were added giving a final 19.4% H_2O^{18} content in the 0.1 M triflic acid solution and a second experiment with a 9.7% H_2O^{18} content. Online MS was then carried out analysing the generation of the three O_2 isotopes, namely, $^{32}O_2$, $^{34}O_2$ and $^{36}O_2$ and the results are summarized in Table 3. Three possible scenarios are considered: a) a fast exchange process of the Ru–O oxygen atom, b) a WNA mechanism and c) a bimolecular coupling of two Ru–O units that is named, I2M.[32] In case of a fast exchange

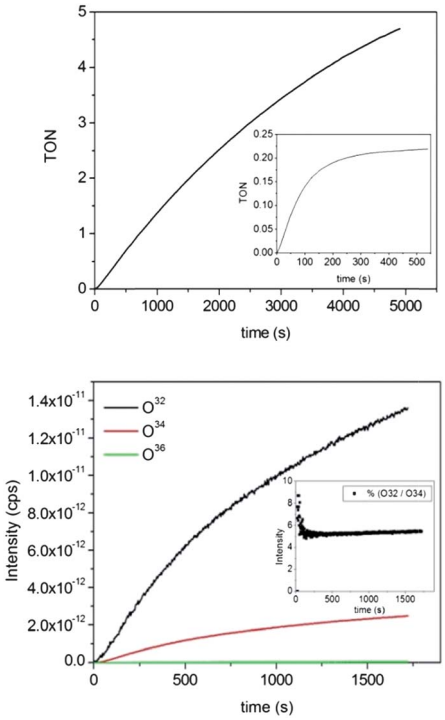

Fig. 5 O_2 evolution profiles. Top, manometry $\mathbf{1}^{2+}$: Ce(IV) (1 : 100). The inset shows the manometry using $\mathbf{1}^{2+}$: Ce(IV) (1 : 4.1). Bottom, on line MS monitoring of O_2 isotopes (32, 34 and 36) with 19.4% solvent labelling. Inset $[O_2{}^{32}]/[O_2{}^{34}]$ ratio over time.

process no mechanistic information could be extracted regarding the O–O formation event. The relative concentrations of the three isotopes clearly show that in this system the only operative mechanism that is occurring is a water nucleophilic attack. Even though WNA is a widely proposed mechanism it is only the first time that has been proved with a mononuclear mono-aqua Ru complex. Previously we showed that the mononuclear bis-aqua complex *cis*-$[Ru^{II}(bpy)_2(H_2O)_2]^{2+}$ also underwent a WNA mechanism based on labelling experiments.[34c] Previous evidence invoked to support WNA for mononuclear Ru-aqua complexes involves mainly kinetic experiments. There are also labelling experiments reported for the blue dimer, $\{[Ru^{III}(bpy)_2(H_2O)]_2(\mu\text{–}O)_2\}^{4+}$,[36] although in this instance a combination of paths besides WNA are proposed to occur simultaneously.

Quantum chemical calculations

To characterize the water oxidation mechanism of $\mathbf{1}^{2+}$ in more detail, we performed DFT calculations at the M06-L level of theory using the SMD continuum solvation model to account for bulk aqueous solvation effects (full cycle in Scheme 1). We also employed CASSCF/CASPT2 calculations for the DFT optimized structures for compound $\mathbf{1}^{2+}$ and its more highly oxidized analogues in order better to characterize the detailed electronic structure of the Ru–O moieties in the various oxidation states.

We began with $[Ru^{II}\text{–}OH_2]^{2+}$ and examined two consecutive steps that, combined, result in the formation of $[Ru^{IV}\text{–}O]^{2+}$. The calculated redox potentials at pH = 1.0 are 0.46 V and 0.75 V, respectively, for the $[Ru^{III}\text{–}OH_2]^{3+}/[Ru^{II}\text{–}OH_2]^{2+}$ and $[Ru^{IV}\text{–}O]^{2+}/[Ru^{III}\text{–}OH_2]^{3+}$ couples, in fair agreement with the experimentally observed values of 0.83 V and >0.97 V (see Table 1). DFT calculations involving continuum solvation models have been

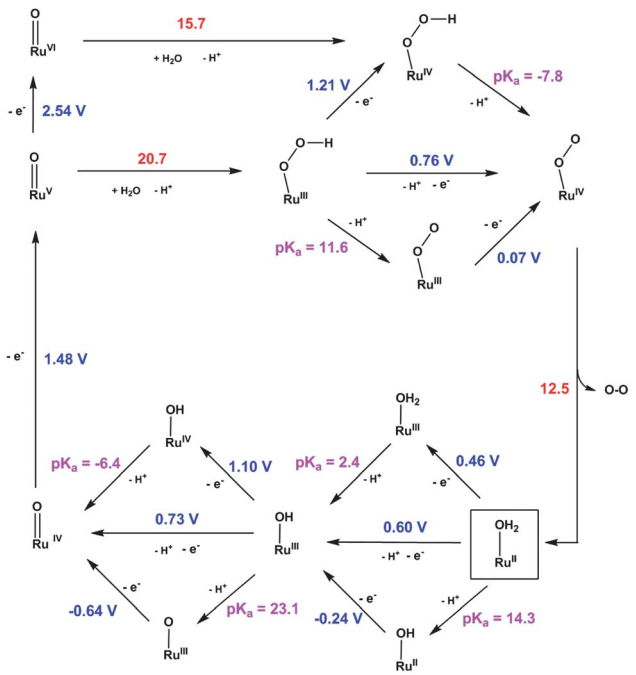

Scheme 1 Catalytic cycle for $[Ru^{II}(damp)(bpy)(OH_2)]^{2+}$ predicted from M06-L calculations; free energy values in kcal mol^{-1}, electrochemical potentials in volts, and pK_a values in log units.

Table 3 Relative isotopic ratios of O_2 evolved from catalyst $\mathbf{1}^{2+}$, along with the calculated values assuming different reaction mechanisms

		Isotopic ratios				
Entry	^{18}O labelling [%][a]	O_2	Exch.[b]	WNA[c]	I2M[d]	Exp.
1	19.4	$^{16}O_2$	65.0	80.4	99.5	84.3
2		$^{16}O^{18}O$	31.3	19.5	0.5	15.4
3		$^{18}O_2$	3.8	0.05	6×10^{-4}	0.3
4	9.7	$^{16}O_2$	81.5	90.1	99.5	89.7
5		$^{16}O^{18}O$	17.6	9.8	0.5	10.3
6		$^{18}O_2$	0.9	0.1	6×10^{-4}	0

[a] Degree of solvent ^{18}O labelling. [b] Exch.: expected ratios in the case of a fast O atom exchange between the catalyst and the solvent. [c] WNA: expected ratios for the mechanism involving a water nucleophilic attack from the solvent to a Ru–O group. [d] I2M: expected ratios for the mechanism involving a bimolecular interaction of two Ru–O groups.

shown often to be accurate to within 100 mV for reduction potentials, and we and others have had good success in prior studies of transition metal containing systems.[16a,37] The prediction of pK_a values using continuum solvation approaches has also been studied extensively[37,38] and we offer a conservative estimate of error for this process of about 300 mV. As PCET free energy changes implicitly include both electron and proton transfer steps (the proton and electron-transfers involved in these PCET steps are expected to proceed at diffusion controlled rates), a worst-case error estimate is on the order of 400 mV. Our calculations in this study display deviations from the experimental values on the order of this error estimate, which prompted us to look more closely at the likely source of the largest error. For the $[Ru^{III}–OH_2]^{3+}/[Ru^{II}–OH_2]^{2+}$ couple, as there is no change in chemical formula, it is straightforward to use CASPT2 electronic energies in place of those from the M06-L level of theory, in which case we predict a reduction potential of 0.72 V *vs.* NHE, which is in considerably better agreement with experiment (the same comparison cannot be made for the second couple as there is not a consistent complete active space for the oxidized and reduced species). This finding suggests that the DFT level of theory may be systematically underestimating, by about 250 mV (*vide infra*), the energetic cost to oxidize these complexes. Based on these observations we carried out several calculations to investigate this point and noticed a significant dependence on the choice of basis set for the calculated redox potentials. For instance, using the same ANO type basis sets as used for the CASPT2 calculations, we found that the calculated M06-L redox potentials agree with the experimental ones to within 100 mV; however, ANO type basis sets with triple ζ quality on all atoms increase the error margin up to 300 mV. This observation will merit attention in future studies of metal-catalyzed water oxidation reactions.

In terms of electronic structure, both at the DFT and CASSCF/CASPT2 levels of theory, $[Ru^{II}–OH_2]^{2+}$ has a closed-shell singlet ground state, $[Ru^{III}–OH]^{2+}$ has a doublet ground state, and $[Ru^{IV}–O]^{2+}$ has a triplet ground state. As a formal Ru^{IV}=O species, the oxo group in $[Ru^{IV}–O]^{2+}$ might be thought to be susceptible to nucleophilic attack by a water molecule. However, our attempts to locate a transition-state (TS) structure for this process were unsuccessful as the approach of a water molecule to the oxo group was found to be repulsive at all distances, even in the presence of additional explicit water molecules provided to assist in proton translocation from the nucleophilic water molecule as part of O–O bond formation (*cf.* below discussion). The lack of WNA reactivity observed here for $[Ru^{IV}–O]^{2+}$ is consistent with the high barriers predicted for WNA in a bimetallic compound containing $[Ru^{IV}–O]^{2+}$ moieties,[34a,39] and we speculate based on accumulating evidence that in general $[Ru^{IV}–O]^{2+}$ fragments will fail to be productive for O–O bond formation through a WNA-type mechanism.

Following this observation, we considered a possible additional oxidation of $[Ru^{IV}–O]^{2+}$ to $[Ru^{V}–O]^{3+}$ or, ultimately, $[Ru^{VI}–O]^{4+}$ species. The calculated reduction potential for the first oxidation is 1.48 V at the M06-L level and 1.72 V *vs.* NHE at the CASPT2 level (again, the DFT level appears to be underestimating the oxidation cost compared to CASPT2, which compares more favourably to experiment). This step is thus predicted to occur spontaneously with CAN as the sacrificial oxidant. However, subsequent oxidation to $[Ru^{VI}–O]^{4+}$ is predicted to require 2.54 V at the M06-L level, which is clearly far outside the range of spontaneity.

We thus proceeded next to consider WNA for the $[Ru^{V}–O]^{3+}$ structure, which has a doublet electronic ground state, and we successfully located a pentamolecular transition-state structure (also doublet), which combines proton transfer from the attacking water to an adjacent set of water molecules with concomitant O–O bond formation (Fig. 6). The free energy of activation for this step was predicted to be 20.7 kcal mol^{-1} with respect to separated $[Ru^{V}–O]^{3+}$ and reactant water molecules. While the inclusion of fewer water molecules might have been expected to reduce the activation barrier from the standpoint of reduced entropy of assembly, we found that with fewer water molecules the proton translocation mechanism was insufficiently advanced, leading to either higher activation free energies, or an inability to find a TS structure at all. This is likely to be an ongoing challenge in quantum chemical modelling of water activation catalysts—it is becoming increasingly clear that the first and perhaps other solvation shells may play a decisive role in proton transfer as part of O–O bond formation steps.[34,40] The resulting hydroperoxo intermediate, $[Ru^{III}–OOH]^{2+}$ is also a doublet from which the open-shell singlet $[Ru^{IV}–OO]^{2+}$ species can be formed following either stepwise or concerted paths for PCET (Scheme 1). Based on the computed energetics for proton loss, it appears that this step either follows or proceeds in concert with electron transfer. In the final step of the mechanism O_2 is released by water displacement at the ruthenium center of the resulting $[Ru^{IV}–OO]^{2+}$, thereby regenerating the initial catalyst $[Ru^{II}–OH_2]^{2+}$. We predict this step to proceed with a free energy of activation of 12.5 kcal mol^{-1}.

Thus for complex $\mathbf{1}^{2+}$ the WNA step is rate determining and based on this, catalyst improvement should involve ligand design that could reduce the barrier for this step. Options would include increasing the electrophilicity of the $[Ru^{V}–O]^{3+}$ moiety through ligand modification, *e.g.*, fluorination, provided that such modification does not move the reduction potential outside of an accessible range. Another alternative might be to provide a general base as an extension of the ligand to assist in water deprotonation.

However, as suggested in Table 1, the nature of the rds can change significantly depending on the auxiliary ligands that

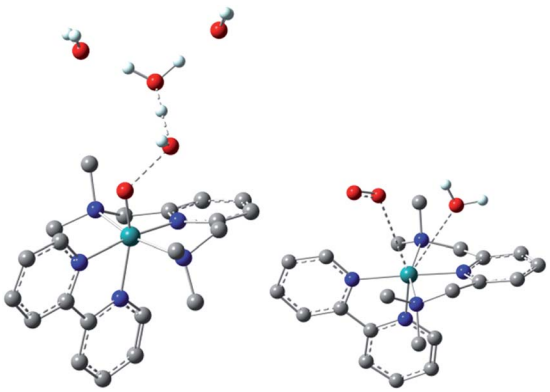

Fig. 6 M06-L transition-state structures for O–O bond formation (left) and O_2 liberation (right).

complete the coordination sphere of the Ru metal center, due to the availability of multiple pathways. As a consequence of this, the prediction of a potential mechanism based only on the electronic nature of the auxiliary ligands is practically impossible. For instance, for complex $\mathbf{5}^{2+}$, containing the MeO-bpy ligand, the metal based oxidation of $[Ru^{IV}{=}O]^{2+}$ to $[Ru^{V}{=}O]^{3+}$ is fast as expected due to the strong electron donating nature of the MeO group (see Table 1). For the same reason the metal reduction of $[Ru^{IV}–OO]^{2+}$ to $[Ru^{II}–H_2O]^{2+}$ with generation of O_2 is slow. However in this case the rds is proposed to be the one electron oxidation of $[Ru^{IV}–OO]^{2+}$ to form $[Ru^{V}–OO]^{3+}$ which is from an electronic point of view totally counterintuitive, given the relatively fast kinetics associated with the $[Ru^{IV}{=}O]^{2+}$ to $[Ru^{V}{=}O]^{3+}$ process. Further, for complex $\mathbf{3}^{2+}$, with the strong electron withdrawing bpm ligand, the rds is proposed to be a metal reduction process, $[Ru^{IV}–OO]^{2+} + H_2O \rightarrow [Ru^{II}–OH_2]^{2+} + O_2$, which is again counterintuitive. The complexity of these systems is also illustrated for complex $\mathbf{2}^{2+}$, where the kinetic analysis shows that at pH = 1.0 the rds is first order in [Ru] and zero in [Ce(IV)]. However when the kinetic analyses are done at pH = 0.0 then the rds is first order both in Ce(IV) and Ru, which illustrates the delicate balance that exists between pH, redox potentials and the accessibility of different reaction paths.

To close this section, we turn from theoretical analysis of the reaction mechanism to a more detailed examination of the electronic structure of the Ru=O fragment in the variously oxidized intermediates. This work complements the results from X-ray absorption spectroscopy presented above and provides a means for quantification of oxidation within the Ru=O fragment itself.

Table 4 presents data for the two aquo compounds involved in the first oxidation step couple, as well as data predicted for the oxo compounds of the formal Ru^{IV}, Ru^{V}, and Ru^{VI} species. The formal Ru^{VI} compound is not predicted to be accessible with CAN as oxidant, but it is nevertheless instructive to consider its electronic structure.

The aquo compounds are provided primarily to afford some context for the population analysis methods. The $[Ru^{II}–OH_2]^{2+}$ and $[Ru^{III}–OH_2]^{3+}$ molecules have singlet and doublet wave functions, respectively, each of which is entirely dominated by a single configuration (*i.e.*, the Hartree–Fock wave function). They have effective Ru–O bond orders of 1, as expected, and inspection of the Ru and OH_2 fragment partial charges indicates that the LoProp model distributes substantial positive charge onto the remaining ligand framework, but oxidation of the Ru–OH_2 fragment itself is predicted to occur essentially exclusively at Ru, that is, the OH_2 fragment charge is effectively unchanged on going from $[Ru^{II}–OH_2]^{2+}$ to $[Ru^{III}–OH_2]^{3+}$. CASSCF Mulliken spin populations computed for the $[Ru^{III}–OH_2]^{3+}$ species also indicate essentially all of the spin to be on Ru (0.969) rather than O (0.001), consistent with expectations for a Ru^{III} compound.

Considering next the $[Ru^{IV}–O]^{2+}$ oxo compound, it is predicted to have a triplet ground state (that is reasonably single configurational) and an effective bond order just below 2. This is associated with an electronic structure that is reminiscent of molecular oxygen, with one doubly occupied σ orbital and two doubly occupied π orbitals between the two atoms, as well as two *singly* occupied π* orbitals. However, the difference in electronegativities between the Ru and O atoms also makes the bond quite polar, with predicted charges of 1.257 and −0.452, respectively (the remaining charge resides on the damp ligand). Interestingly, the magnitude of the Ru partial charge is not much different from that predicted for $[Ru^{III}–OH_2]^{3+}$. Similarly, CASSCF Mulliken spin population analysis indicates a dominant oxyl character with 0.961 electrons localized on O and 1.011 on Ru. While it is risky to make quantitative comparisons of charges in molecules having different stoichiometry and *total* charge, nevertheless the computed charges and spin densities are consistent with the XAS analysis above, which suggests some Ru^{III} character in a $[Ru^{IV}{=}O \leftrightarrow Ru^{III}–O^{\bullet}]$ valence bond formulation. Analogous results have been reported by Anxolabéhère-Mallart *et al.*,[41] who analyzed DFT calculations, XANES pre-edge features, and reactivity results for a formal Mn^{IV}-oxo species and concluded that it was better characterized as a Mn(III)-oxyl compound.

One electron oxidation to $[Ru^{V}–O]^{3+}$ removes an electron in one of the π* orbitals, which has the expected effect of increasing the bond order by 0.5 and changing the electronic state to a doublet. Note that *both* the Ru and O partial atomic charges are predicted to increase, by about 0.3 a.u. for Ru and 0.23 a.u. for O. Thus, increased oxidation is spread across the full Ru–O fragment, albeit it is predicted to be somewhat more prevalent at the Ru terminus than the O alternative. Consistent with that observation, the spin density of the doublet is significantly delocalized over both the Ru (0.574) and O (0.394) atoms. Such behaviour has been previously noted for high oxidation states of dioxo-Ru(bpy)$_2$ based on XAS spectroscopy and CASSCF/CASPT2 calculations.[42]

Consideration of these results, and reports for many other water oxidation catalysts,[43,34a,c] suggests that some hole character on O is critical to lowering the activation free energies for water nucleophilic attack to values of about 20 kcal mol^{-1} or below.

Continuing this trend, further oxidation to Ru^{VI} removes the remaining π* electron, generating a singlet state with the bond order increased to 2.6, and in this instance more partial positive charge is added to the O than to the Ru, indicative of the degree to which Ru is resistant to ever further oxidation. While such increased hole character on oxygen is consistent with the lower barrier predicted for water nucleophilic attack on $[Ru^{VI}–O]^{4+}$ (Scheme 1), the very positive standard reduction potential predicted for this unobserved couple places it outside the thermodynamically accessible range.

Table 4 Effective bond orders (unitless) and LoProp partial atomic charges (a.u.) from CASSCF wave functions for various intermediates

Compound	$<S^2>$	Weight[a]	Eff. bond order	q_{Ru}/q_O
$[Ru^{II}–OH_2]^{2+}$	0.00	99% (6,5)	1.0	0.834/−0.647[b]
$[Ru^{III}–OH_2]^{3+}$	0.75	97% (5,5)	1.0	1.320/−0.668[b]
$[Ru^{IV}–O]^{2+}$	2.00	90% (10,8)	1.8	1.257/−0.452
$[Ru^{V}–O]^{3+}$	0.75	87% (9,8)	2.3	1.552/−0.219
$[Ru^{VI}–O]^{4+}$	0.00	79% (8,8)	2.6	1.714/0.010

[a] Weight of dominant configuration state function in CAS wave function for indicated space (of active electrons, active orbitals). [b] Sum of oxygen and proton charges for H_2O fragment.

Conclusions

As a final conclusion and given the complexity of the systems studied, it is important to enlarge the number of experimental

and theoretical analyses for water oxidation catalysts in order to be able to understand the different parameters that drive the complex to a particular pathway. In particular it is very important to understand how the electronic perturbations affect the redox potentials together with the understanding of the nature of the electronic structure of the higher oxidation state species and intermediates. In this respect the use of formal oxidation states is useful for electron counting purposes, but it is obvious that for oxidation states higher than Ru(III) the oxidation process also involves the oxygen atom bonded to the metal centre. Therefore the degree of oxo *vs.* oxyl nature of the reactive oxygen atom also plays a crucial role that up to now escapes easy *a priori* rationalisation and thus precludes a straightforward prediction of a reaction mechanism.

Acknowledgements

Support from MICINN (CTQ2010-21497 and Consolider Ingenio CSD2006-0003), Generalitat de Catalunya (CIRIT/2009 SGR 69) and the WCU Program (R31-10010) Korea, are gratefully acknowledged. NP is grateful for a MICINN doctoral grant. MH thanks the Deutsche Forschungsgemeinschaft for a Heisenberg-Fellowship and for funding (grant Ha3265/3-1). We thank Dr Maarten Nachtegaal at the SuperXAS beamline of SLS for excellent technical support. CJC thanks the US National Science Foundation (CHE09-52054). HD thanks the UniCat cluster of excellence (Unifying Concept in Catalysis, Berlin) for support.

Notes and references

1 http://www.alt-energy.info/hydrogen-power/hondas-home-hydrogen-fueling-station/. January 24th, 2008.
2 http://www.naikontuning.com/noticias_nt/2011/05/13/audi-balanced-mobility-el-e-gas-project-a-metano/. May 13th, 2011.
3 (*a*) L. Schlapbach and A. Züttel, *Nature*, 2001, **414**, 353; (*b*) H. Lee, J.-W. Lee, D. Y. Kim, J. Park, Y.-T. Seo, H. Zeng, I. L. Moudrakovski, C. I. Ratcliffe and J. A. Ripmeester, *Nature*, 2005, **434**, 743.
4 (*a*) N. Armaroli and V. Balzani, *Angew. Chem., Int. Ed.*, 2007, **46**, 52; (*b*) S. His, "Hydrogen: An Energy Vector for the Future", *Panorama*, 2004, IFP-Information, France; (*c*) J. S. Connolly, *"Photochemical Conversion and Storage of Solar Energy"*. Academic Press, New York, 1981; (*d*) M. Grätzel, *"Energy Resources through Photochemistry and Catalysis*, Academic Press, New York, 1983; (*e*) T. N. Verziroglu and F. Barbir, *Int. J. Hydrogen Energy*, 1992, **17**, 391.
5 (*a*) B. Radaram, J. A. Ivie, W. M. Singh, R. M. Grudzien, J. H. Reibenspies, C. E. Webster and X. Zhao, *Inorg. Chem.*, 2011, **50**, 10564–10571; (*b*) S. Roeser, P. Farràs, F. Bozoglian, M. Martínez-Belmonte, J. Benet-Buchholz and A. Llobet, *Chem. Sus. Chem.*, 2011, **4**, 197; (*c*) L. Bernet, R. Lalrempuia, W. Ghattas, H. Mueller-Bunz, L. Vigara, A. Llobet and M. Albrecht, *Chem. Commun.*, 2011, **47**, 8058; (*d*) R. Lalrempuia, N. D. McDaniel, H. Müller-Bunz, S. Bernhard and M. Albrecht, *Angew. Chem., Int. Ed.*, 2010, **49**, 9765; (*e*) J. D. Blakemore, N. D. Schley, D. Balcells, J. F. Hull, G. W. Olack, C. D. Incarvito, O. Eisenstein, G. W. Brudvig and R. H. Crabtree, *J. Am. Chem. Soc.*, 2010, **132**, 16017; (*f*) W. C. Ellis, N. D. McDaniel, S. Bernhard and T. J. Collins, *J. Am. Chem. Soc.*, 2010, **132**, 10990; (*g*) D. J. Wasylenko, C. Ganesamoorthy, J. Borau-Garcia and C. P. Berlinguette, *Chem. Commun.*, 2011, **47**, 4249; (*h*) L. Duan, L. Tong, Y. Xu and L. Sun, *Energy Environ. Sci.*, 2011, **4**, 3296.
6 (*a*) Z. Chen, J. J. Concepcion, H. Luo, J. F. Hull, A. Paul and T. J. Meyer, *J. Am. Chem. Soc.*, 2010, **132**, 17670; (*b*) D. J. Wasylenko, C. Ganesamoorthy, M. A. Henderson, B. D. Koivisto, H. D. Osthoff and C. P. Berlinguette, *J. Am. Chem. Soc.*, 2010, **132**, 16094; (*c*) S. Romain, F. Bozoglian, X. Sala and A. Llobet, *J. Am. Chem. Soc.*, 2009, **131**, 2768.
7 S. Roeser, M. Z. Ertem, C. Cady, R. Lomoth, J. Benet-Buchholz, L. Hammarstrom, B. Sarkar, W. Kaim, C. J. Cramer and A. Llobet, *Inorg. Chem.*, 2012, **51**, 320.
8 H. Dau, P. Liebisch and M. Haumann, *Anal.Bioanal. Chem.*, 2003, **376**, 562.
9 S. I. Zabinsky, J. J. Rehr, A. L. Ankudinov, R. C. Albers and M. J. Eller, *Phys. Rev. B: Condens. Matter*, 1995, **52**, 2995.
10 (*a*) Y. Zhao and D. G. Truhlar, *J. Chem. Phys.*, 2006, **125**, 194101; (*b*) Y. Zhao and D. G. Truhlar, *Acc. Chem. Res.*, 2008, **41**, 157–167; (*c*) Y. Zhao and D. G. Truhlar, *Theor. Chem. Acc.*, 2008, **120**, 215.
11 D. Andrae, U. Haeussermann, M. Dolg, H. Stoll and H. Preuss, *Theor. Chim. Acta*, 1990, **77**, 123.
12 W. J. Hehre, L. Radom, P. V. R. Schleyer, J. A. Pople, *Ab Initio Molecular Orbital Theory*, Wiley, New York, 1986.
13 C. J. Cramer, *Essentials of Computational Chemistry: Theories and Models*, 2nd ed., John Wiley & Sons, Chichester, 2004.
14 A. V. Marenich, C. J. Cramer and D. G. Truhlar, *J. Phys. Chem. B*, 2009, **113**, 6378.
15 (*a*) M. D. Tissandier, K. A. Cowen, W. Y. Feng, E. Gundlach, M. H. Cohen, A. D. Earhart, J. V. Coe and T. R. Tuttle, *J. Phys. Chem. A*, 1998, **102**, 7787; (*b*) D. M. Camaioni and C. A. Schwerdtfeger, *J. Phys. Chem. A*, 2005, **109**, 10795; (*c*) C. P. Kelly, C. J. Cramer and D. G. Truhlar, *J. Phys. Chem. B*, 2006, **110**, 16066; (*d*) V. S. Bryantsev, M. S. Diallo and W. A. Goddard, *J. Phys. Chem. B*, 2008, **112**, 9709.
16 (*a*) A. Lewis, J. A. Bumpus, D. G. Truhlar and C. J. Cramer, *J. Chem. Educ.*, 2004, **81**, 596 (erratum 2007, **84**, 934); (*b*) P. Winget, C. J. Cramer and D. G. Truhlar, *Theor. Chem. Acc.*, 2004, **112**, 217.
17 (*a*) T. Ziegler, A. Rauk and E. J. Baerends, *Theor. Chim. Acta*, 1977, **43**, 261; (*b*) L. Noodleman, *J. Chem. Phys.*, 1981, **74**, 5737; (*c*) C. J. Cramer and D. G. Truhlar, *Phys. Chem. Chem. Phys.*, 2009, **11**, 10757.
18 (*a*) K. Yamaguchi, F. Jensen, A. Dorigo and K. N. Houk, *Chem. Phys. Lett.*, 1988, **149**, 537; (*b*) T. Soda, Y. Kitagawa, T. Onishi, Y. Takano, Y. Shigeta, H. Nagao, Y. Yoshioka and K. Yamaguchi, *Chem. Phys. Lett.*, 2000, **319**, 223.
19 For comparison purposes Ru bond distances in Angstroms of X-ray and DFT (in parenthesis) calculated structures are indicated. Ru–O, 1.805 (1.759); Ru-damp: Ru–N_{py}, 1.991 (2.008), Ru–N_{tert}, 2.177 (2.206) and 2.151 (2.121); Ru-bpy: Ru–N, 2.088 (2.117) and 2.164 (2.201).
20 (*a*) L. Noodleman, C. Y. Peng, D. A. Case and J.-M. Mouesca, *Coord. Chem. Rev.*, 1995, **144**, 199; (*b*) I. Ciofini and C. A. Daul, *Coord. Chem. Rev.*, 2003, **238–239**, 187; (*c*) J. N. Harvey, *Struct. Bonding*, 2004, **112**, 151; (*d*) F. Neese, *Coord. Chem. Rev.*, 2009, **253**, 526.
21 (*a*) B. O. Roos, P. R. Taylor and P. E. M. Siegbahn, *Chem. Phys.*, 1980, **48**, 157; (*b*) K. Andersson, P.-Å. Malmqvist and B. O. Roos, *J. Chem. Phys.*, 1992, **96**, 1218.
22 F. Aquilante, L. De Vico, N. Ferre, G. Ghigo, P. A. Malmqvist, P. Neograd, T. B. Pedersen, M. Pitonak, M. Reiher, B. O. Roos, L. Serrano-Andres, M. Urban, V. Veryazov and R. Lindh, *J. Comput. Chem.*, 2010, **31**, 224.
23 B. A. Hess, *Phys. Rev. A: At., Mol., Opt. Phys.*, 1986, **33**, 3742.
24 (*a*) B. O. Roos, R. Lindh, P. A. Malmqvist, V. Veryazov and P. O. Widmark, *J. Phys. Chem. A*, 2005, **109**, 6575; (*b*) B. O. Roos, R. Lindh, P. A. Malmqvist, V. Veryazov and P. O. Widmark, *J. Phys. Chem. A*, 2004, **108**, 2851.
25 L. Gagliardi, R. Lindh and G. Karlström, *J. Chem. Phys.*, 2004, **121**, 4494.
26 (*a*) B. O. Roos, A. C. Borin and L. Gagliardi, *Angew. Chem., Int. Ed.*, 2007, **46**, 1469; (*b*) M. Brynda, L. Gagliardi and B. O. Roos, *Chem. Phys. Lett.*, 2009, **471**, 1.
27 T. W. Welch, S. A. Ciftan, P. S. White and H. H. Thorp, *Inorg. Chem.*, 1997, **36**, 4812.
28 D. J. Wasylenko, C. Ganesamoorthy, M. A. Henderson and C. P. Berlinguette, *Inorg. Chem.*, 2011, **50**, 3662.
29 (*a*) J. Concepcion, J. W. Jurss, J. L. Templeton and T. J. Meyer, *J. Am. Chem. Soc.*, 2008, **130**, 16462; (*b*) G. Zhang, R. Zong, H. W. Tseng and R. P. Thummel, *Inorg. Chem.*, 2008, **47**, 990.
30 J. Concepcion, J. W. Jurss, M. R. Norris, Z. Chen, J. L. Templeton and T. J. Meyer, *Inorg. Chem.*, 2010, **49**, 1277.
31 S. Masaoka and K. Sakai, *Chem. Lett.*, 2009, **38**, 182.
32 S. Romain, L. Vigara and A. Llobet, *Acc. Chem. Res.*, 2009, **42**, 1944.

33 Specfit is a trademark of Spectrum Software Associates.

34 (*a*) F. Bozoglian, S. Romain, M. Z. Ertem, T. K. Todorova, C. Sens, J. Mola, M. Rodríguez, I. Romero, J. Benet-Buchholz, X. Fontrodona, C. J. Cramer, L. Gagliardi and A. Llobet, *J. Am. Chem. Soc.*, 2009, **131**, 15176; (*b*) A. Sartorel, P. Miró, E. Salvadori, S. Romain, M. Carraro, G. Scorrano, M. Di Valentin, A. Llobet, C. Bo and M. Bonchio, *J. Am. Chem. Soc.*, 2009, **131**, 1651; (*c*) X. Sala, M. Z. Ertem, L. Vigara, T. K. Todorova, W. Chen, R. C. Rocha, C. J. Cramer, L. Gagliardi and A. Llobet, *Angew. Chem., Int. Ed.*, 2010, **49**, 7745.

35 K. J. Takeuchi, M. S. Thompson, D. W. Pipes and T. J. Meyer, *Inorg. Chem.*, 1984, **23**, 1845.

36 (*a*) D. Geselowitz and T. J. Meyer, *Inorg. Chem.*, 1990, **29**, 3894; (*b*) C. W. Chronister, R. A. Binstead, J. Ni and T. J. Meyer, *Inorg. Chem.*, 1997, **36**, 3814; (*c*) R. A. Binstead, C. W. Chronister, J. Ni, C. M. Hartshorn and T. J. Meyer, *J. Am. Chem. Soc.*, 2000, **122**, 8464; (*d*) H. Yamada, W. F. Siems, T. Koike and J. K. Hurst, *J. Am. Chem. Soc.*, 2004, **126**, 9786.

37 (*a*) P. Winget, C. J. Cramer and D. G. Truhlar, *Theor. Chem. Acc.*, 2004, **112**, 217; (*b*) P. Winget, E. J. Weber, C. J. Cramer and D. G. Truhlar, *Phys. Chem. Chem. Phys.*, 2000, **2**, 1231; (*c*) M. H. Baik and R. A. Friesner, *J. Phys. Chem. A*, 2002, **106**, 7407; (*d*) M. Uudsemaa and T. Tamm, *J. Phys. Chem. A*, 2003, **107**, 9997; (*e*) P. Jaque, A. V. Marenich, C. J. Cramer and D. G. Truhlar, *J. Phys. Chem. C*, 2007, **111**, 5783; (*f*) Y. Shimodaira, T. Miura, A. Kudo and H. Kobayashi, *J. Chem. Theory Comput.*, 2007, **3**, 789; (*g*) I. Chiorescu, D. V. Deubel, V. B. Arion and B. K. Keppler, *J. Chem. Theory Comput.*, 2008, **4**, 499; (*h*) D. Schultz, F. Biaso, A. R. M. Shahi, M. Geoffroy, K. Rissanen, L. Gagliardi, C. J. Cramer and J. R. Nitschke, *Chem.–Eur. J.*, 2008, **14**, 7180; (*i*) C. J. Cramer and D. G. Truhlar, *Acc. Chem. Res.*, 2008, **41**, 760; (*j*) A. Galstyan and E. W. Knapp, *J. Comput. Chem.*, 2009, **30**, 203; (*k*) M. Namazian, C. Y. Lin and M. L. Coote, *J. Chem. Theory Comput.*, 2010, **6**, 2721; (*l*) Y. Zhao and D. G. Truhlar, *Rev. Mineral. Geochem.*, 2010, **71**, 19; (*m*) J. T. York, A. Llobet, C. J. Cramer and W. B. Tolman, *J. Am. Chem. Soc.*, 2007, **129**, 7990.

38 (*a*) C. P. Kelly, C. J. Cramer and D. G. Truhlar, *J. Phys. Chem. A*, 2006, **110**, 2493; (*b*) J. M. Ho and M. L. Coote, *Theor. Chem. Acc.*, 2010, **125**, 3; (*c*) K. S. Alongi, G. C. Shields, *Annual Reports in Computational Chemistry*, R. Wheeler, Ed., Elsevier, Dordrecht, 2010, 6, p. 113.

39 X. Yang and M.-H. Baik, *J. Am. Chem. Soc.*, 2008, **130**, 16231.

40 (*a*) L. P. Wang, Q. Wu and T. Van Voorhis, *Inorg. Chem.*, 2010, **49**, 4543; (*b*) R. Bianco, P. J. Hay and J. T. Hynes, *J. Phys. Chem. A*, 2011, **115**, 8003.

41 B. Lassalle-Kaiser, C. Hureau, D. A. Pantazis, Y. Pushkar, R. Guillot, V. K. Yachandra, J. Yano, F. Neese and E. Anxolabéhère-Mallart, *Energy Environ. Sci.*, 2010, **3**, 924.

42 N. Planas, L. Vigara, C. Cady, P. Miró, P. Huang, L. Hammarström, S. Styring, N. Leidel, H. Dau, M. Haumann, L. Gagliardi, C. J. Cramer and A. Llobet, *Inorg. Chem.*, 2011, **50**, 11134.

43 (*a*) M. Z. Ertem, L. Gagliardi and C. J. Cramer, *Chem. Sci.*, 2012, **3**, 1293; (*b*) X. C. Li, G. J. Chen, S. Schinzel and P. E. M. Siegbahn, *Dalton Trans.*, 2011, **40**, 11296; (*c*) L. P. Wang and T. Van Voorhis, *J. Phys. Chem. Lett.*, 2011, **2**, 2200.

